Asian Journal of Civil Engineering (2018) 19:205–221
https://doi.org/10.1007/s42107-018-0018-3

ORIGINAL PAPER

Comparison of aerodynamic coefficients of setback tall buildings due to wind load

Amlan Kumar Bairagi[1] · Sujit Kumar Dalui[1]

Received: 29 November 2017 / Accepted: 1 February 2018 / Published online: 8 February 2018
© Springer International Publishing AG, part of Springer Nature 2018

Abstract
Irregular and unsymmetrical buildings are the modern trend for architectural and structural engineers, and this type of structure is always taken special care to design. This study focuses on the comparison between two setback buildings. Pressure, force, and torsional moment coefficients are highlighted in this study. The suction at the roof top of single-side setback is 95.84% higher than the both-side setback model. Torsional moment of both-side setback model is 259.02% higher than the single-side setback model. This study says that the both-side setback model is more susceptible than the single-side setback model.

Keywords Stepped shape building · Roof setback · Computational fluid dynamics (CFD) · Pressure coefficient · Force coefficient · Torsional moment coefficient

Introduction

Unconventional and irregular shape tall buildings are holding impressive positions in present scenario. The taper, helical, and setback, opening at tall buildings are captivating structure according to the architectural point of view. Therefore, the environmental loads are taking most critical factor on the structure. Especially, the wind loads are taking the leading sector for tall buildings. Therefore, structural safety is also taking the vital part on the building. Kareem (1992) presented the results of a dynamic response of high-rise buildings due to wind, and also focused across the wind and torsional components of aerodynamic loads and their statistical correlations with different aspect ratios. Kijewski-Correa and Pirnia (2007) found and suggested (the need for time frequency analyses on dynamic behavior of tall buildings.under wind and also highlighted the effect of damping values as well as the comparatively larger degree of energy dissipation. Mendis et al. (2007) enumerated simple quasi-static treatment of wind load on tall buildings. Irwin et al. (2008) established the energy in tall building increased with the increase the height of a tall building. When the width of the building decreased by tapering or setbacks, then the vortices also tried to shade the different frequencies at different heights; at the same time, fluctuation forces are also reduced. Kim et al. (2008) carried out for three aeroelastic, tapered, tall building models with taper ratios of 5, 10, and 15% and one basic model of a square cross section without a taper were tested using wind tunnel test which simulated the suburban environment. Tanaka et al. (2013) studied the aerodynamic response due to wind and flow characteristics of tall buildings with 34 numbers unconventional shapes in wind tunnel test and computational fluid dynamics (CFD) simulation, and setback model is one of them. Shiva et al. (2013) highlighted the study and described the value of base shear and twisting moment on five different tall building models with steps near its top and highlights the influence of steps at the top of the building model. Xie (2014) studied aerodynamic optimization of super-tall buildings and its effectiveness assessment on tapering, twisting, and stepping, and tried to minimize the conflict between optimization scheme and the other design aspects. Mendis et al. (2014) discussed a number of

✉ Amlan Kumar Bairagi
bairagiak@gmail.com; mohammadnejad@birjandut.ac.ir

[1] Department of Civil Engineering, Indian Institute of Engineering Science and Technology, Shibpur, Howrah, India

problems, mistakes, and solutions for CFD wind analysis. That study also touches the limitations in wind design code and wind tunnel testing also. Baby et al. (2015) presented an overview of the optimal external shape and structural system for tall buildings subject to aerodynamic loads and the response of a structure through a comprehensive investigation of the building of different cross section based on the CFD results. Xu and Xie (2015) focused the aerodynamic optimization of tall buildings and best compromise wind issues. The authors introduce a method to assess the effectiveness of optimization by tapering, stepping, or twisting building elevations that takes use of sectional aerodynamic data derived from a simple wind tunnel pressure testing. Masera et al. (2015) documented two case studies were presented to show how the wind loads are calculated and applied in the design. The first case study is based on the CFD results for the New Marina Casablanca Tower in Casablanca, Morocco. The second case study considers the results from the wind tunnel test studies conducted for the Al-Hamra tower in Kuwait City. Roy and Bairagi (2016) discussed wind pressure and force coefficients on stepped tall building at different geometrical shape placed on above to each other like rectangular, square, and triangular. Velocity around the model for different wind angles is also highlighted here. Elshaer et al. (2016) conferred the improvement of the aerodynamic performance of tall buildings which conducted by adopted and developed aerodynamic optimization procedure (AOP). After that CFD, optimization algorithm and artificial neural network (ANN) models are used to reliably predict the optimal building shape. Tamura et al. (2017) conferred pedestrian-level and aerodynamic wind characteristics of super-tall buildings with various configurations and conducted the dynamic wind response.

This study focuses the connection of pressure coefficient, force coefficient, torsional moment coefficient, and roof pressure variations between two setback buildings which have setbacks at half height of the building. The buildings are the same square plan area and same setback area of roof at half height. The models are analyzed by CFD simulation for attacking wind angle 0° to 180° at 15° interval. Incredible change of torsional moment and roof pressure is detected due to change of setback position from one side to two different sides of the building. This study also tried to clarify the change of pressure and twisting moment, which helps to better design for setback building.

Theoretical background

Computational fluid dynamics (CFD) is a part of fluid mechanics and it creates a virtual simulation of wind tunnel and creates a data structure to solve the fluid flows. CFD is very convenient tools and grand alternative of the wind tunnel. A number of methods are available in CFD to forecast the wind effect. The k–ε model is broadly used segment in CFD. The gradient diffusion hypothesis is used in k–ε models to relate the Reynolds stresses to the mean velocity gradients and the turbulent viscosity. With the help of ANSYS CFX-solver theory guide (2012), Eqs. (1)–(7) are stated. The turbulent viscosity modelled as the merchandise of a turbulent velocity and turbulent length scale. k is the turbulence kinetic energy and is defined as the variance of the fluctuations in velocity. It has dimensions of (L^2T^2); for example, m^2/s^2. ε is the turbulent eddy dissipation and has dimensions of per unit time (L^2T^3); for example, m^2/s^3. The k–ε model introduces two new variables into the system of equations. The continuity equation is such an example:

$$\frac{\partial \rho}{\partial t} + \frac{\partial}{\partial x_j}\left(\rho U_j\right) = 0. \tag{1}$$

Moreover, the momentum equation will be

$$\frac{\partial \rho U_i}{\partial t} + \frac{\partial}{\partial x_j}\left(\rho U_i U_j\right) = -\frac{\partial p'}{\partial x_i} + \frac{\partial}{\partial x_j}\left[\mu_{\text{eff}}\left(\frac{\partial U_i}{\partial x_j} + \frac{\partial U_i}{\partial x_I}\right)\right] + S_{\text{M}}, \tag{2}$$

where S_{M} = sum of body forces; μ_{eff} = effective viscosity accounting for turbulence; p' = modified pressure as defined by the following:

$$p + \frac{2}{3}\rho k + \frac{2}{3}\mu_{\text{eff}}\frac{\partial U_{\text{k}}}{\partial k}. \tag{3}$$

The last term in Eq. (3), i.e., $\left(\frac{2}{3}\mu_{\text{eff}}\frac{\partial U_{\text{k}}}{\partial k}\right)$ is involves the divergence of velocity. It neglected in CFX. Therefore, this assumption is strictly correct only for incompressible fluids. The k–ε model is based on the eddy viscosity concept, so that:

$$\mu_{\text{eff}} = \mu + \mu_{\text{t}}, \tag{4}$$

where μ_t is the turbulent viscosity.

The k–ε model assumes that the turbulence viscosity linked to the turbulence kinetic energy and dissipation via the relation:

$$\mu_{\text{t}} = C_\mu \rho \frac{k^2}{\varepsilon}. \tag{5}$$

The values of k and ε come directly from the differential transport equations for the turbulence kinetic energy and turbulence dissipation rate:

$$\frac{\partial(\rho k)}{\partial t}+\frac{\partial}{\partial x_j}\left(\rho k U_j\right)=\frac{\partial}{\partial x_j}\left[\left(\mu+\frac{\mu_t}{\sigma_k}\right)\frac{\partial k}{\partial x_j}\right] + P_k + P_b - \rho\varepsilon - Y_M + S_k \tag{6}$$

$$\frac{\partial(\rho\varepsilon)}{\partial t}+\frac{\partial}{\partial x_j}\left(\rho\varepsilon U_j\right)=\frac{\partial}{\partial x_j}\left[\left(\mu+\frac{\mu_t}{\sigma_\varepsilon}\right)\frac{\partial\varepsilon}{\partial x_j}\right]+\rho C_1 S_\varepsilon - \rho C_2\frac{\varepsilon^2}{k+\sqrt{v\varepsilon}}+C_{1\varepsilon}\frac{\varepsilon}{k}C_{3\varepsilon}P_b+S_\varepsilon, \tag{7}$$

where

$$C_1=\max\left[0.43,\frac{\eta}{\eta+5}\right],\quad \eta=S\frac{k}{\varepsilon},\quad S=\sqrt{2S_{ij}S_{ij}}.$$

Here, P_k = the generation of turbulence kinetic energy due to the mean velocity gradients; P_b = the generation of turbulence kinetic energy due to buoyancy; Y_M = the contribution of the fluctuating dilatation in compressible turbulence to the overall dissipation rate; where, k–ε turbulence model constant $C_{1\varepsilon}=1.44$, k–ε turbulence model constant $C_2=1.92$, Turbulence model constant for the k equation $\sigma_k=1.0$ and k–ε turbulence model constant $\sigma_\varepsilon=1.2$.

Description of models

The building models, namely Model A1 and Model A2, have the same plan area of length $(L)=250$ mm, breadth $(B)=250$ mm, and height $(H)=500$ mm. Building setback has been placed at level $H/2$ for both the models, but have some difference. For model A1, the setback distance is $0.2L=50$ mm from the one vertical face; similarly, for model A2, they have $0.1L=25$ mm from both opposite vertical faces. Therefore, the setback roof area for model A1 at one side is equally distributed on model A2 on both opposite sides. Analysis of the study is done using CFD simulation for wind incidence angle 0° to 180° at 15° interval. Both the models have flow parallel to Y-axis is 0° and parallel to X is 90°. The model A1 has symmetry about YZ plane and model A2 is about YZ and XZ planes. Therefore, the attacking wind angles are considered from 0° to 180° at 15° interval for model A1 and 0° to 90° at 15° interval for model A2. Face names A, B, C, D1, D2 and roofs R1, R2 are used for model A1; similarly, for model A2, they have face A, B1, B2, C, D1, D2 and roof RD1, RB1, and R2. Detail modes are shown in Fig. 1.

Methodology

CFD simulation has been done for two different setback bluff body. The setback was placed at the half height of the building. Two models have the same base dimension (L and B) and height (H). The side ratio (L/B) was unity. Aspect ratio between top and bottom dimensions (L/L_1) = 1.25 and height-to-length ratio (H/L) = 2. The regions of fluid flow and/or heat transfer in CFX are called domains. Fluid domains define a region of fluid flow, while solid domains are regions occupied by conducting solids in which volumetric sources of energy can be specified. The typical steps adopted in ANSYS CFX are described under the flow diagram under Fig. 2.

Boundary condition

The numerical study carried out by CFD simulation adopting with the same boundary condition for both the models. A conventional square plan shape tall building has the same plan dimension and height which are simulated in the same domain to validate the study with the different international codes. The inlet, lateral, and top boundary considered $5H$ (H = building height) from the model and outflow boundary should be placed at $15H$ behind the model to allow for proper flow development recommended by Frank et al. (2004), Revuz et al. (2012). The direction constraint requires that the flow direction is parallel to the boundary surface normal that calculated at each element face on the inlet boundary. For no slip wall (not moving, no wall velocity), the velocity of the fluid at the wall boundary is set to zero, so the boundary condition for the velocity becomes $U_{wall}=0$. For free slip wall, the velocity component parallel to the wall has a finite value, but the velocities normal to the wall and the wall shear stress are both set to zero: $U_{wall}=0$, $\tau_w=0$. The velocity profile of the atmospheric boundary layer in the CFD is calculated by the following power law:

$$\frac{U}{U_H}=\left(\frac{Z}{Z_H}\right)^{\alpha}, \tag{8}$$

where U is the horizontal wind speed at an elevation Z; U_H is the speed at the reference elevation Z_H; which was 10 m/s; α is the parameter that varies with ground roughness that is 0.133 for terrain category 2 and Z_H is 1.0 m. The kinetic energy of turbulence and its dissipation rate at the inlet section is calculated according to the following equations:

$$k=\frac{3}{2}\left(U_{avg}I\right)^2 \quad\text{and}\quad \varepsilon=C_\mu^{3/4}\left(\frac{k^{3/2}}{l}\right), \tag{9}$$

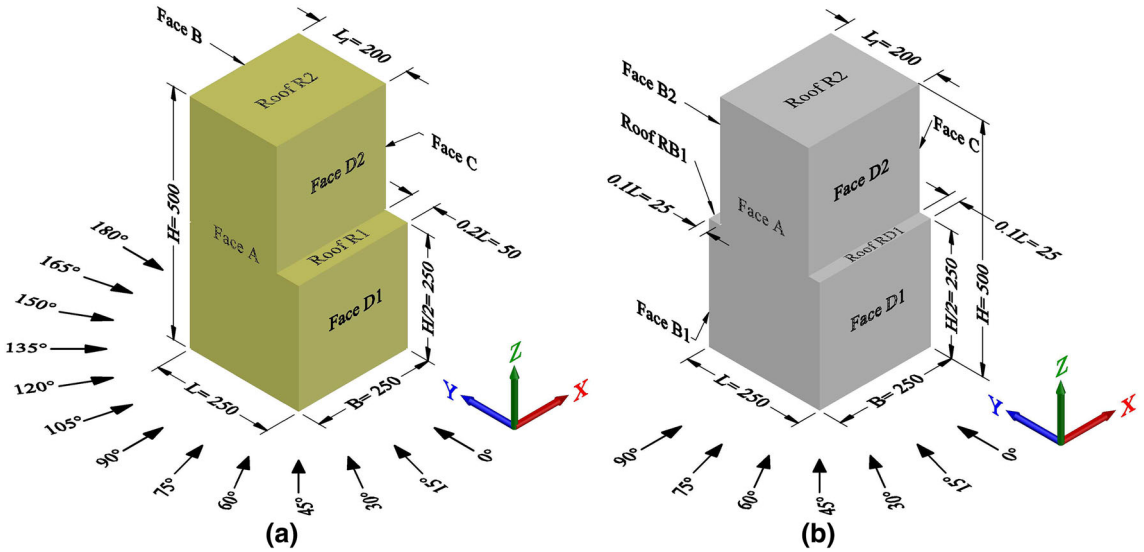

Fig. 1 Dimension, face name, and wind angle details for **a** model A1 and **b** model A2

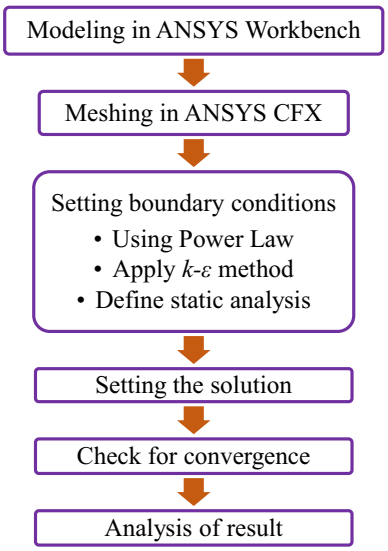

Fig. 2 Flowchart of ANSYS CFX to solve the simulation of analytical model

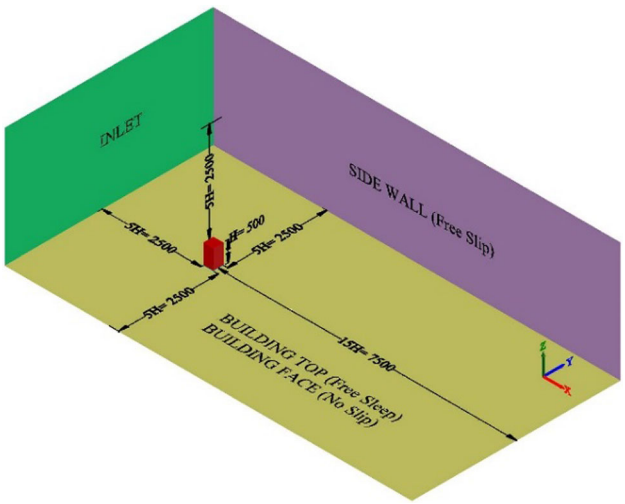

Fig. 3 Computational domain and boundary conditions

where U_{avg} is the mean velocity at the inlet; I is the turbulence intensity; l is the turbulence integral length scale. Normal air temperature 25 °C considered in the domain and k–ε turbulence model. Building walls are no slip condition but sidewall, building top and top of the domain is free slip condition, as shown in Fig. 3.

Meshing of computational model

Mesh adaptation in CFX is the process in which, once or more during a run, the mesh is selectively refined in areas that depend on the adoption criteria specified. This means that as the solution is calculated, the mesh can automatically be refined in locations where solution variables are hanging most rapidly, to resolve the features of the flow in these regions. The tetrahedron meshing used and inflated near the boundary. This meshing is used for all models in CFD simulation to avoid the unusual flows. Fine meshing is used for the models for better results. Meshing of the conventional square plan shape tall building, $0.2L$ and $0.1L$ setback building models with domain is also shown under Fig. 4. Long section of meshing for model A1 and model A2 is shown in Fig. 5

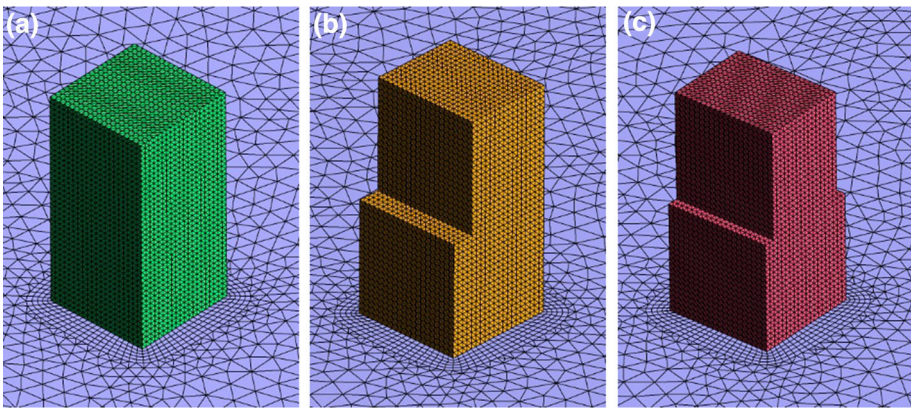

Fig. 4 Meshing of different buildings and domain: **a** conventional square plan shape tall building, **b** stepped model with 0.2L setback distance, and **c** stepped model with 0.1L setback distance

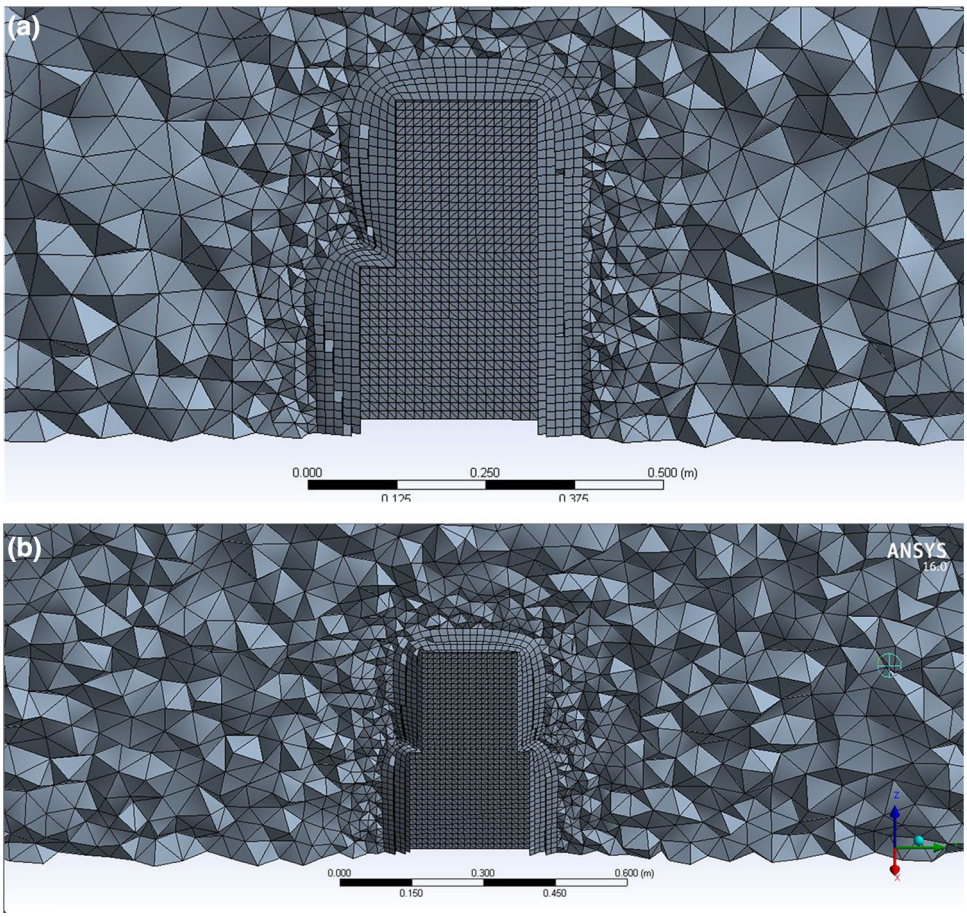

Fig. 5 Long section of meshing showing discretization of mesh for **a** model A1 and **b** model A2

Authentication of analytical study

Model 2 has been verified with Kim and Kanda (2013) and the paper based on experimental study which was conducted in Eiffel-type wind tunnel (1.8 m × 1.8 m × 12.5 m) at the University of Tokyo. Four tall building models were used and setback model also one of them. The full-scale square plan area model has bottom dimension 40 m and top dimension 24 m; the height of building 160 m and setback distance 8 m. The side ratio was unity, and aspect ratio between top and bottom dimension was four. The assumed length scale was 1:400 and 15% turbulence intensity. The power law exponent was 0.13. Considered wind angles are 0° to 180° with 15° intervals. The CFD simulation has been made according to this configuration and compared with the experimental study. The validation of turbulence intensity and mean wind speed between experimental and analytical

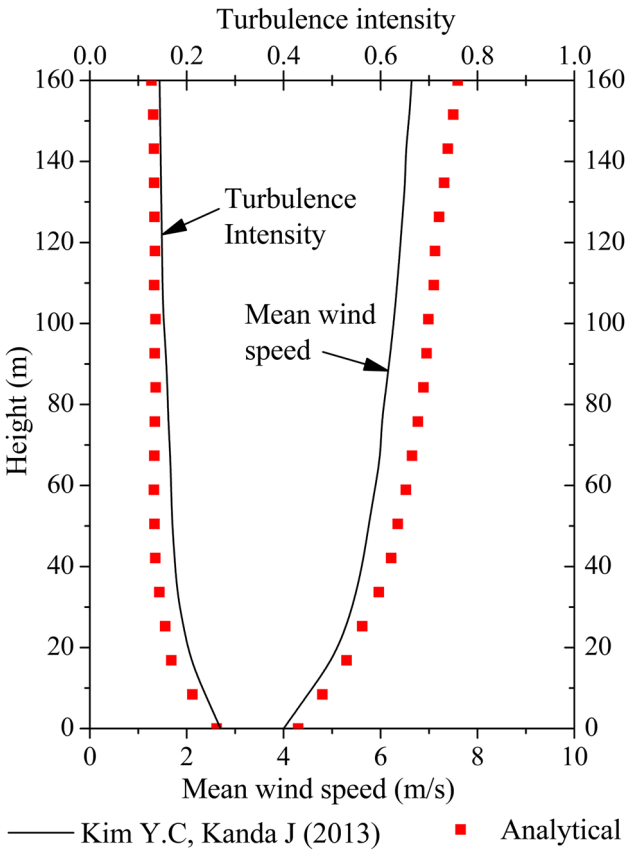

Fig. 6 Comparison of experimental and analytical study for turbulence intensity and mean wind speed

studies is highlighted under Fig. 6. From this figure, it is clear that the turbulence intensity and mean wind speed for analytical study are followed by the experimental study. Again, the largest mean pressure coefficient for setback model is 0.80 for experimental and 0.833 for analytical study of 0° wind. In addition, smallest coefficient is − 1.08 for experimental and − 1.105 for experimental study for 90° wind. This validation says that the analytical study follows the experimental study. Therefore, the analytical results are also acceptable for the design purpose.

Conventional square plan shape tall building

Pressure distribution on the conventional square plan shape tall building

A conventional square plan shape with uniform cross-sectional tall building having comparison with stepped model is considered to validate this study in using CFD simulation. The conventional square plan shape model has $L = 250$ mm, $B = 250$ mm, $H = 500$ mm and the same plan area (62,500 mm^2) related with both model A1 and A2. This building abides 0° wind at face A which is parallel to X-axis and 90° wind angle at face D which is parallel to Y-axis, as shown in Fig. 7a. As the symmetry in plan about X- and Y-axes, the nature of C_p at face A due to 0° wind should be the same for 90° wind at face D. When the building withstanding 0° wind angle, face A, and face C responded as windward and leeward face with positive pressure and negative pressure, respectively. At the same time, face B and D skilled with suction. Velocity profile has been drawn at the inlet position of the square plan shape building and this profile is the same as stated in S.P 64 (S&T):2001 (2001) see Fig. 7b. Kwon and Kareem (2013) also focused the comparative study of major international wind codes and standards for wind effects on tall buildings. Weerasuriya and Jayasinghe (2014) evaluated the wind load on high-rise building using five major international wind codes in both ultimate and serviceability limit conditions. The results of pressure coefficients are validated with table: 5, IS 875: part 3 (2015) (Indian Standard) according to the aspect ratio ($h/w = 2$ and $l/w = 1$) of the model and the force coefficients are also obtained from Fig. 4 of the same code. The square model from CFD analysis is also compared with the AS/NZS: 1170.2 (2002) (Australia/New Zealand standard), ASCE/SEI 7-10 (2010) (American standard), EN: 1991-1-4 (2005) (European standard), BS: 6399-2 (1997) (British standard), as shown in Tables 1 and 2. The face name, contour diagrams, and streamline of square plan shape model for 0° wind angle are shown in Fig. 8.

Analytical results for setback models

Widely use CFD package is adopted in this analytical study for the step shaped model A1 and A2. Model A1 has setback 0.2L, i.e., 50 mm from one side and model A2 has setback 0.1L, i.e., 25 mm on two opposite sides. The setback areas for both the buildings are the same and have the same square plan area with the equal aspect ratio for the wind angle 0° to 180° at 15° interval. Comparative study has been done with these two models using the horizontal and vertical pressure coefficient, drag and lift coefficient, and the torsional moment coefficient of the models.

Pressure coefficient for model A1 and A2

Model A1 and A2 have the same dimension of $L = 250$ mm, $B = 250$ mm, and $H = 500$ mm. The setback is at level $H/2 = 250$ mm from base of models.

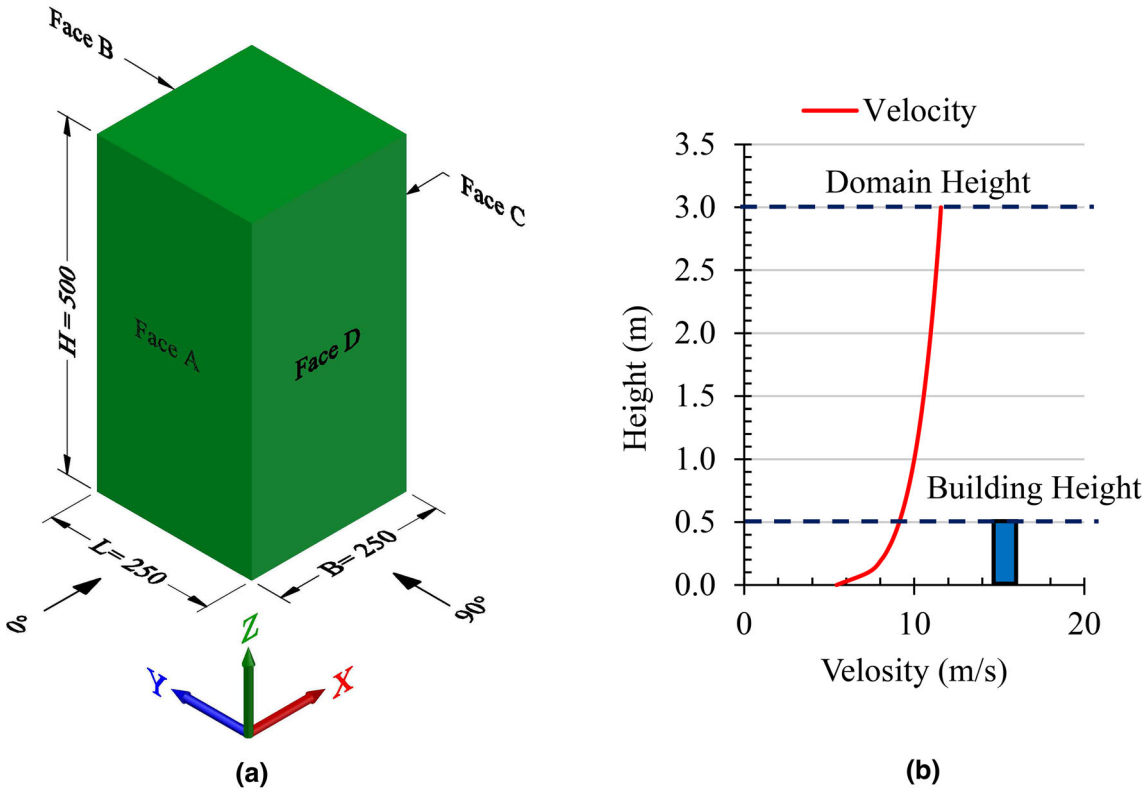

Fig. 7 **a** Square plan shape with uniform cross-sectional tall building showing dimension and face details; **b** velocity profile of square plan shape model for 0° wind angle

Table 1 Comparison of surface pressure coefficient (C_p) on the conventional square plan shape tall building

Location	Pressure coefficient as per											
	ANSYS CFD		AS/NZS: 1170.2:2002		ASCE/SEI 7-10:2010		EN 1991-1-4:2005		BS 6399-2:1997		IS:875 (Part 3)-2015	
	0°	90°	0°	90°	0°	90°	0°	90°	0°	90°	0°	90°
Windward side	0.8	0.8	0.8	0.8	0.8	0.8	0.8	0.8	0.76	0.76	0.8	0.8
Leeward side	− 0.5	− 0.5	− 0.5	− 0.5	− 0.5	− 0.5	− 0.55	− 0.55	− 0.5	− 0.5	− 0.25	− 0.25
Sidewalls	− 0.7	− 0.7	− 0.65	− 0.65	− 0.7	− 0.7	− 0.8	− 0.8	− 0.8	− 0.8	− 0.8	− 0.8

Table 2 Comparison of force coefficient (C_f) on the vertical surface of square plan shape tall building

Force coefficient (C_f) as per				
ANSYS CFD	AS/NZS: 1170.2: 2002	ASCE/SEI 7-10: 2010	EN 1991-1-4:2005	IS:875 (Part 3)-2015
1.28	2.2	1.31	2.1	1.2

Setback distance $0.2L = 50$ mm is set from face D1 for model A1 and setback distance $0.1L = 25$ mm is set to face D1 and B1 for model A2. Therefore, the setback areas for both the models are the same. Horizontal pressure coefficients between model A1 and A2 are correlated in this study. The pressure belts 1–2–3–4 are located at half of the lower part of model A1, i.e., $H/4 = 125$ mm from the base of the model. Similarly, belts 5–6–7–8 are located at ¾th height from the model base, i.e., $3H/4 = 375$ mm. Other two belts, namely, 1′–2′–3′–4′ and 5′–6′–7′–8′, are

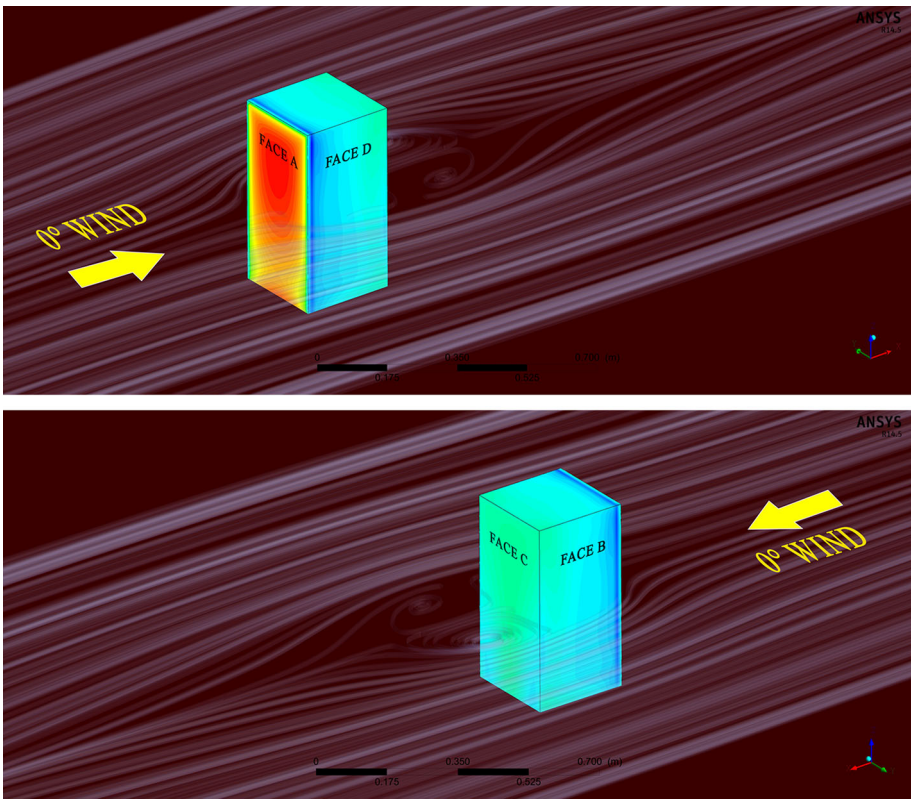

Fig. 8 Face name, contour, and streamline of square plan shape tall building for 0° wind angle

10 mm above and below from H/2 level, i.e., $12H/25 = 240$ mm and $13H/25 = 260$ mm from model base. Another pressure belts a–b–c–d–e–f are used around the vertical perimeter with roof R1 and R2 for model A1 and placed at $B/2 = 125$ mm; however, for model A2, they have two setback roof, therefore the pressure belt a–b–c–d–e–f–g–h are considered at the same B/2 distance, as shown in Fig. 9. As the A1 model has symmetry about YZ plane, therefore, wind angles are set from 0° to 180° at 15° interval and for model A2 have symmetry about YZ and XZ planes; therefore, the angles are 0° to 90° at 15° interval.

Compared results of horizontal face pressure around the model A1 and A2 are highlighted in this section. The model A1 has a setback distance $0.2L$, and therefore, the faces D1 and D2 have different C_p; again, for model A2, they have two setback distances $0.1L$; therefore, faces B1, B2 as well as D1, D2 have different C_p. Considered the average C_p of faces B1, B2 for model A1 to compare the C_p with face B for A2 model, and expressed as B_{avg}. Similarly, faces D1, D2 for both models are expressed as D_{avg}. From Fig. 10a, b, the variation of pressure coefficients of model A2 is almost touching the value of model A1 for 0° wind angle. C_p at face A (− 0.66) are the same for both model A1 and A2 for 0° angle. For 60° angle, face D_{avg} for model A1 changed sign from +0.001 to − 0.006. An interesting criterion noticed for 150° angle. For model A1, face A has high suction (− 0.69) and low suction pressure (− 0.02) for A2 model. This extreme change of pressure is due to the setback of B1 and B2 face for model A2. Horizontal pressure coefficients at level $H/4$, $12H/25$, $13H/25$, and $3H/4$ for 150° angle are also shown under Fig. 11. C_p at starting point 1, 1′, 5′, and 5 at level $H/4$, $12H/25$, $13H/25$, and $3H/4$ are positive for A2 model but suction for A1 model. Positive pressure for A1 model is gradually changing sign between 100 and 200 mm distance from the start point. This pressure difference is due to setback at both sides of model A2.

Vertical pressure coefficient at belts a–b–c–d–e–f for model A1 and a–b–c–d–e–f–g–h for model A2 due to 30° and 150° wind angles are described under Fig. 12a, b. For 30° wind angle, C_p for A1 and A2 are almost the same from start point to 625 mm and create low suction (− 0.36) at 750 mm for A2, whereas A1 has suction (− 0.62). The maximum suction is observed at 1250 mm which is the base of face B. At this location, A1 has (− 0.49) and A2 has (− 0.10) suction value, which denotes that 79.60% suction is decreased from A1 to A2 model due to the setback of model A2 at face B. Vertical C_p for 150° angle is just a mirror image of 30° angle for model A2, but C_p of A1 increased compared with 30° angle for A2 model. For 150° wind, suction difference at start point is (− 0.42) for model A1 and (− 0.10) for A2

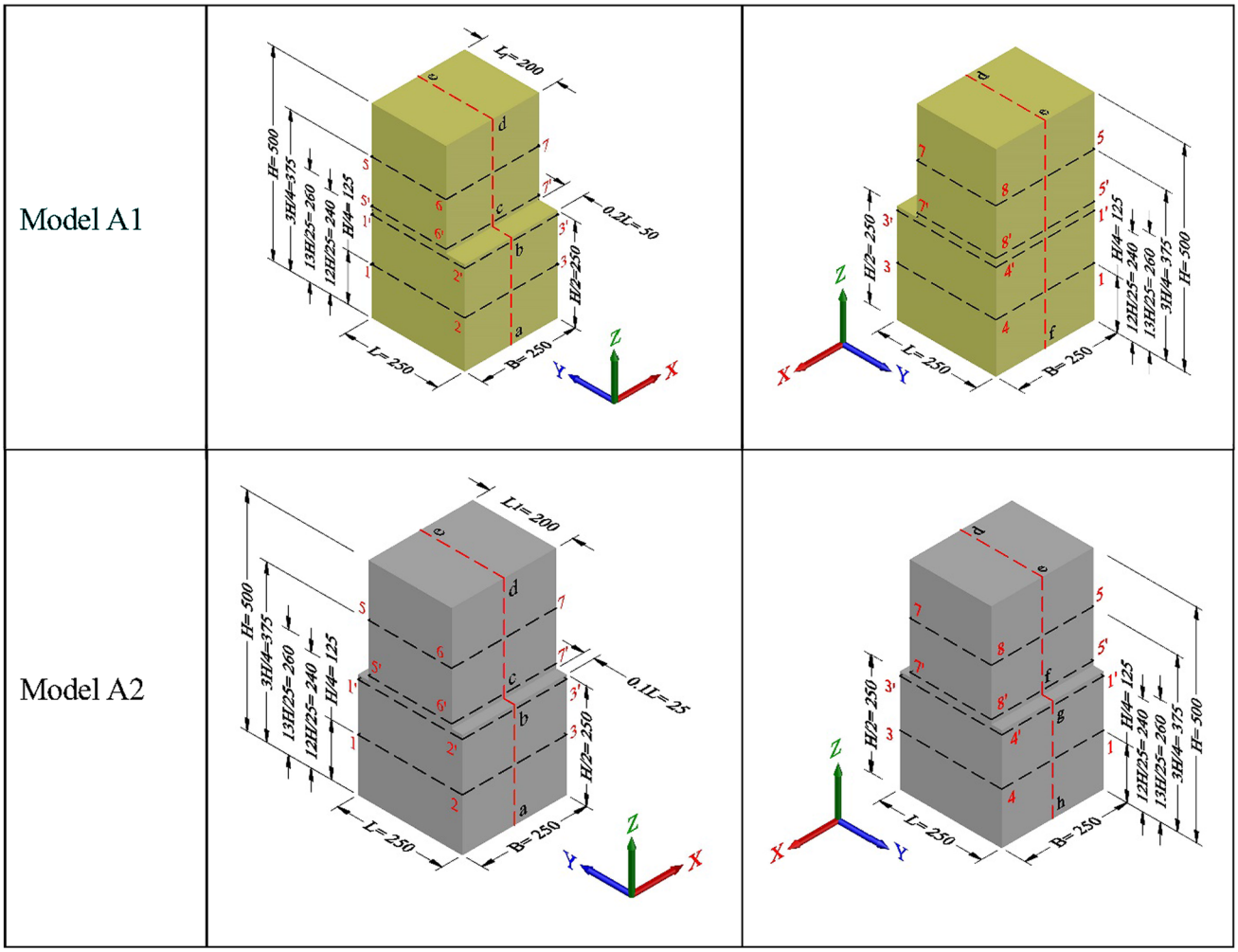

Fig. 9 Diagram shows pressure belts around the building model A1 and A2

model, i.e., 76.19% suction is decreased from A1 to A2 model. Another suction difference is observed at point 702 mm. Model A1 and A2 have suction (− 0.74) and (− 1.10), respectively. Therefore, 48.65% extrasuction developed from A1 to A2 model. On the other hand, the maximum positive pressure difference in location is 861 mm, where C_p for model A1 is (1.15) and for model A2 has (0.93). Therefore, it may be said that C_p has been decreased 19.13% from A1 and A2.

Comparison of pressure contours for the critical angles 30° and 150° for model A1 and 30° for model A2 is also highlighted under Table 3. As the model A2 has two axis of symmetry: therefore, pressure on face A, B1, B2, C, D1 and D2 for wind angle 30° or vice versa for wind angle 150° for model A2. Extreme changes of pressure have been observed on face B (0.68) for model A1 and for the same face (0.59) for model A2. This change is 13.24% compared with the other angles. This face has more pressure drop compared with the face B1 and B2 for model A2. More turbulence has been developed due to the setback on that B face. A remarkable pressure difference of model A1 and A2 has been observed between for 150° and 30° angle on face A. Local pressure also observed at that face for 150° angle. C_p at roof RB1 and R2 for A2 model has a more positive pressure compared with the roof R2 for A1 model at 150° angle, whereas at roof R2 has less suction for A2 compared with the R2 for model A1 due to the less setback roof to model A2. Figure 13a, b also shows the stream lines for 30° and 150° wind for model A1 and Fig. 13c for 30° wind angle for model A2. From this figure, it is clear that high turbulence was developed at faces B1, B2 and roof RB1 due to the setback roof for A2 model.

From Fig. 14a, the pressure coefficient at roof R1 and RD1 is maximum (0.688) and (0.786) for model A1 and

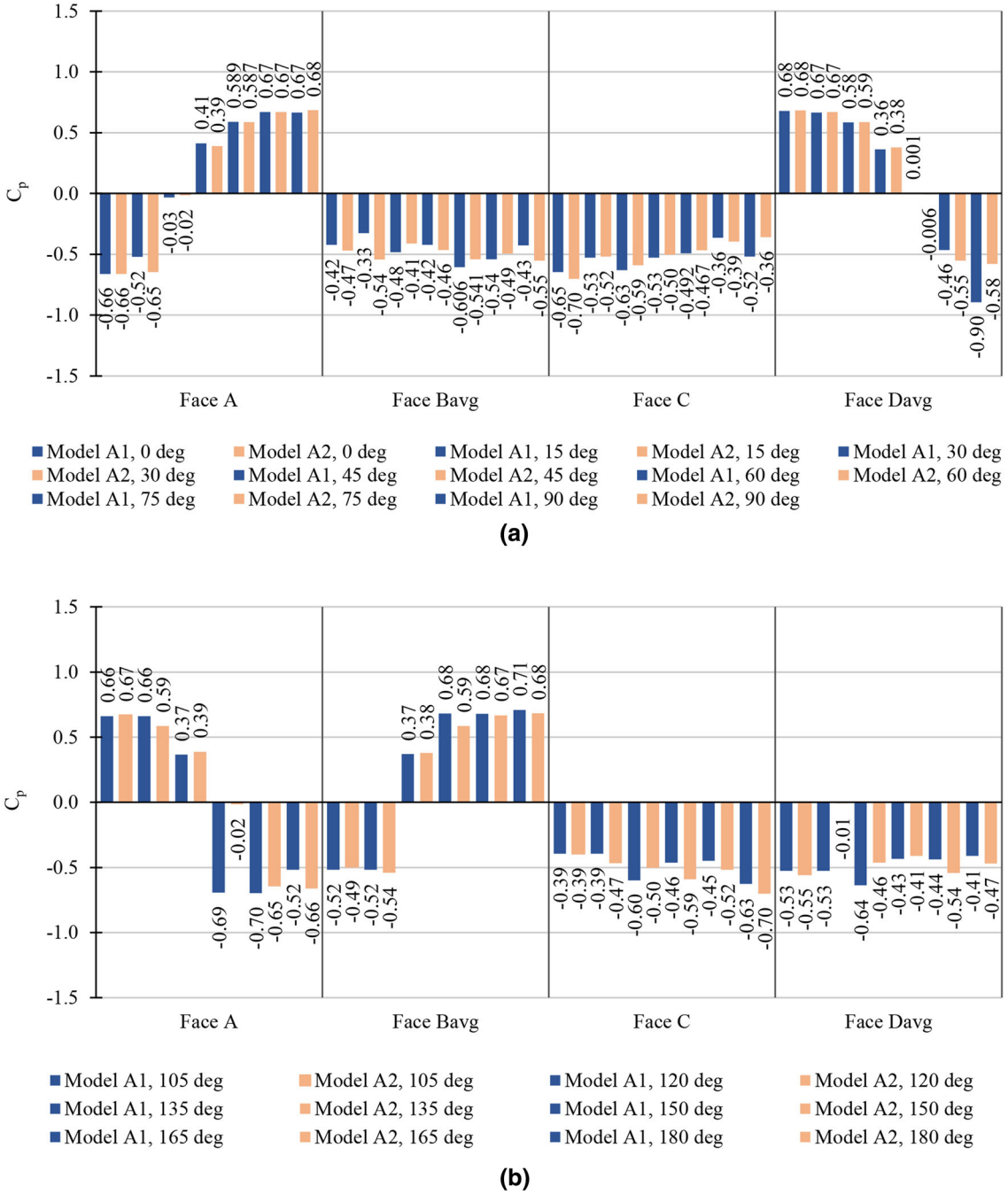

Fig. 10 Comparison of face pressure coefficients for A1 and A2 model due to different wind angles: **a** 0°–90° wind angle and **b** 105°–180° wind angle

A2, respectively, due to 0° angle. Minimum pressure for 90° angle is (− 0.906) and (− 0.632) for R1 and RD1, respectively, and for 150° angle is (− 0.464) and (− 0.656), respectively. Therefore, pressure decreased 14.25% for 0° angle compared to R1 and RD1. Fall of suction compared to R1 and RD1 between both the models is 32.24% for 90° and decrease of the suction is 41.38% for 150° angle. In the same way, C_d is decreased 32.73% from A1 to A2 for 180° angle. A mirror image of a curve for model A2 has been developed in Fig. 14b for RB1 roof, where the maximum and minimum C_p is the same as in RD1 due to the symmetry of model A2. However, roof R2 for both models are suction between 0° to 180°. Maximum suction at roof R2 for model A1 at 135° angle and

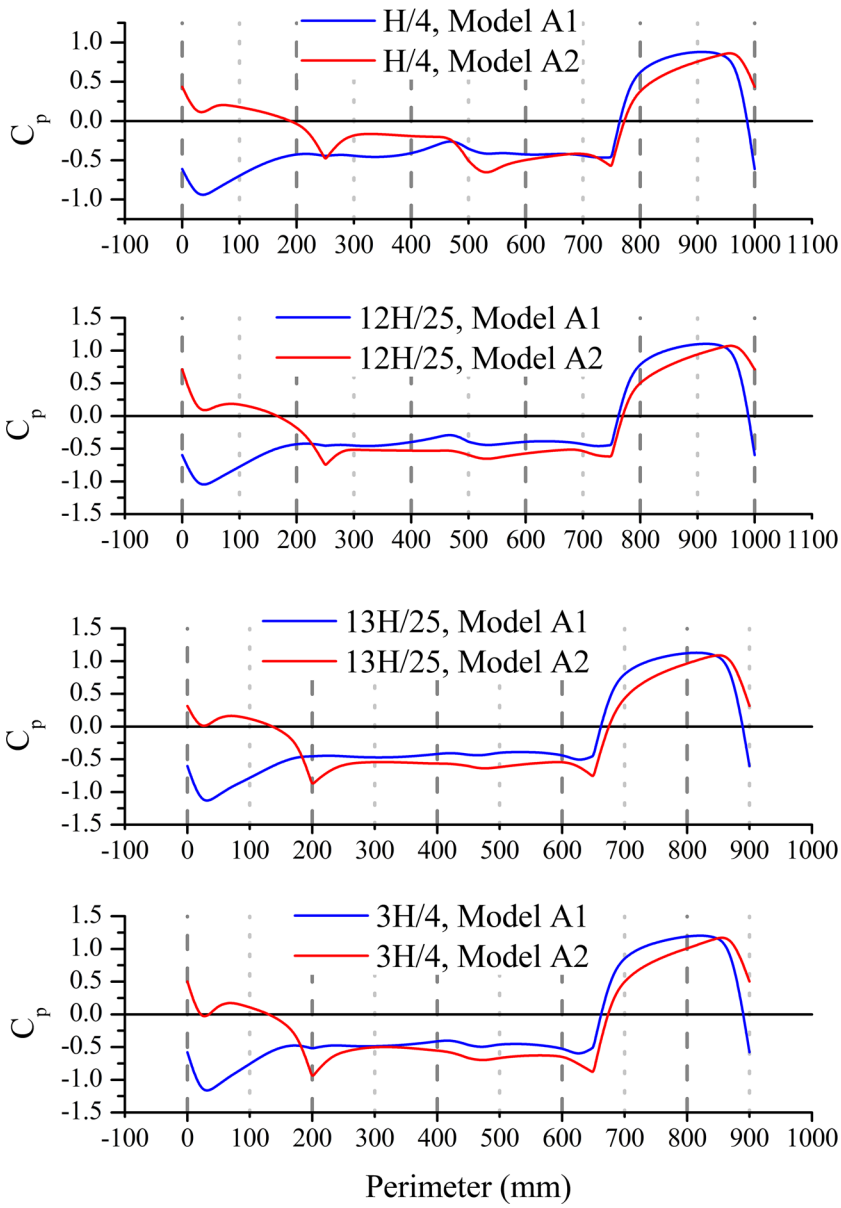

Fig. 11 Comparison of horizontal C_p for 150° wind at belt $H/4$, $12H/25$, $13H/25$, and $3H/4$ for model A1 and A2

minimum suction at roof R2 for model A2 at 90° angle. Similarly, maximum fall of suction compared to R2 between both the models is 27.32% for 90° angle. Therefore, it may be said that model A2 developed less suction for 0°, 90°, and 180° angles compared to model A1 for setback roof and 90° angle for top roof.

Drag, lift, and moment coefficient for model A1 and A2

The lift is the component of total aerodynamic force perpendicular to the direction of flow and drag is the component parallel to the flow direction. In this study, the wind velocity is the same for all the wind angles, but the exposed area of the models is different according to its different wind angles. Therefore, the drag and lift coefficients are also changed according to the wind angles. The torsional moment with respect to the center of gravity of the models is also highlighted in this study. Diagrams of drag, lift, and torsional moment are shown in Fig. 15a. Simiu and Scanlan (1996) discussed the drag coefficient equation:

$$F_D(t) = \frac{1}{2}\rho v^2(t) B^2 C_d, \tag{10}$$

where $F_D(t)$ = the time varying drag on a body, ρ = density of the fluid, $v(t)$ = speed of the object relative to the fluid varying with time, B = typical body dimension, and C_d = drag coefficient.

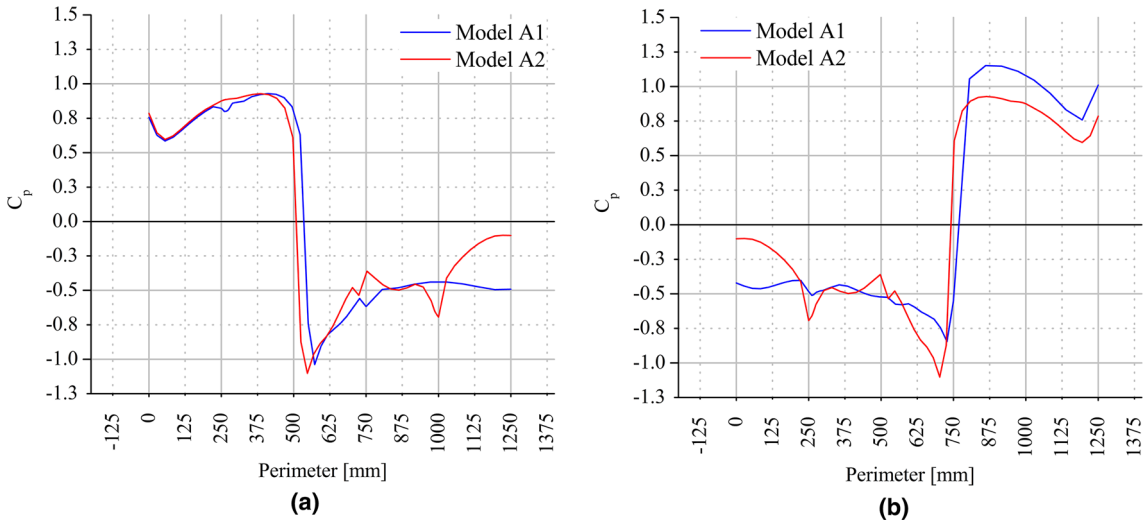

Fig. 12 Comparison of vertical C_p for 30° and 150° wind at belts a–b–c–d–e–f–g–h for model A1 and A2: **a** 30° wind and **b** 150° wind

In this experiment, considering that the square root of body dimension is the exposer area, according to the wind angle, and the equation is satisfying for a particular time only. Therefore, ignore the time variable. Therefore, the above equation will be as follows:

$$F_D = \frac{1}{2}\rho v^2 A C_d. \tag{11}$$

Therefore, the drag coefficient (C_d) may be expressed as follows:

$$C_d = \frac{F_D}{\frac{1}{2}\rho v^2 A} = \frac{F_D}{\frac{1}{2}\rho v^2 B' h}. \tag{12}$$

In addition, lift coefficient (C_l) is as follows:

$$C_l = \frac{F_L}{\frac{1}{2}\rho v^2 A} = \frac{F_L}{\frac{1}{2}\rho v^2 D' h}, \tag{13}$$

where B' = projected width of model normal to wind direction, D' = projected width of model parallel to wind direction, and H = height of the model.

Hossain (2013) discussed lift and drag coefficient on octagonal cross-sectional cylinder and obtained the pressure coefficients by the numerical integration method. Kumar et al. (2016) explore the mean pressure coefficients; drag, lift, and torsional coefficients along and perpendicular to the wind direction are calculated in rectangular model. In this study, the projected length of the model A1 has two parts, upper and lower. Therefore, the term B' also has two parts, namely B'_b for bottom part of the model and B'_t for the top part of the model. The suffix terms denoted the portion of the model like the bottom and top. Similarly, projected width has also two parts like D'_b and D'_t, as shown in Fig. 15b. Therefore, the total projected area may be expressed as $[(B'_b \times h/2) + (B'_t \times h/2)]$ for drag and $[(D'_b \times h/2) + (D'_t \times h/2)]$ for lift. The drag force has been considered from Y axis and lift force from the X-axis. Torsional moment coefficient (C_m) may be expressed as follows:

$$C_m = \frac{M_z}{\frac{1}{2}\rho v^2 A}, \tag{14}$$

where A = projected area of model in wind direction and M_z = calculated moment about base of model.

Drag (C_d), lift (C_l) and torsional moment (C_m) coefficients for model A1 and A2 are projected under Fig. 16a, b, c. Drag force (C_d) is the maximum (1.17) for 0° wind angle (which is parallel to Y axis) for model A1. Furthermore, C_d of face A2 (1.25) is the same for 0° and 180° wind angle, as shown in Fig. 16a. At the same time, the drag force for 90° wind angle is (− 0.02) for A2 model and for A1 is (− 0.48). Which said that the drag force is 95.84% decrease for A1 compared with A2 model. For 180° angle, maximum drag is (1.25) for A2 model and minimum drag is (− 1.17) for A1 model. Therefore, the drag force is 206.84% increased for 180° angle from A1 to A2 model and also change the sign. The maximum lift coefficient (C_l) at 90° angle for A1 is (1.21) and A2 models is (1.14) are very close, i.e., 5.79% increase from A1 model, as shown in Fig. 16b. Minimum lift coefficient for A1 model is (− 0.19) for 165° wind. For 45° wind angle, C_l is (0.65) for A1 and (− 1.07) for A2. As a result, C_l for 45° is decreasing 264.62% from A1 to A2. Similarly, 274.11% for 135° angle and shift sign from positive to negative. Maximum torsional moment (C_m) developed in model A2 (2.19) due to 90° wind angle and for A1 model is (0.61) which denotes that the twisting moment is increasing 259.02% for A2 model for 90° angle as shown in Fig. 16c. For A1 model, it has C_m (1.87) for 180° wind and (− 0.23) for A2 model, so a drop of torsional moment is 112.3%

Table 3 Pressure contour for model A1 and A2 due to 30° and 150° wind angle

Wind angle	Model	Legend	Face A	Face B	Face C	Face D	Roof
30°	Model A1	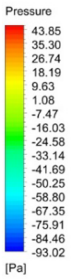	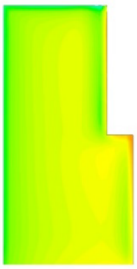	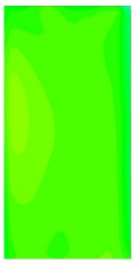		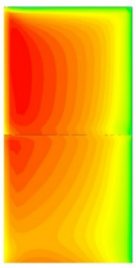	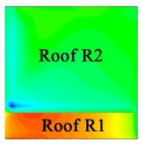
	Model A2					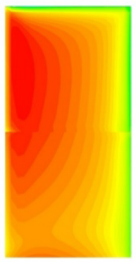	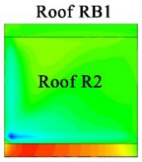
150°	Model A1	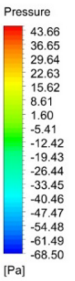	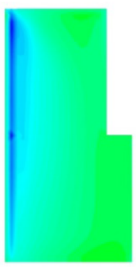	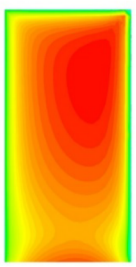			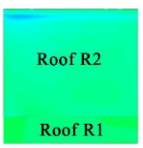
	Model A2			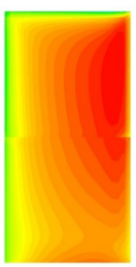		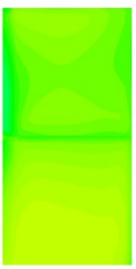	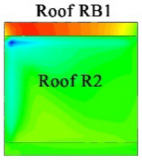

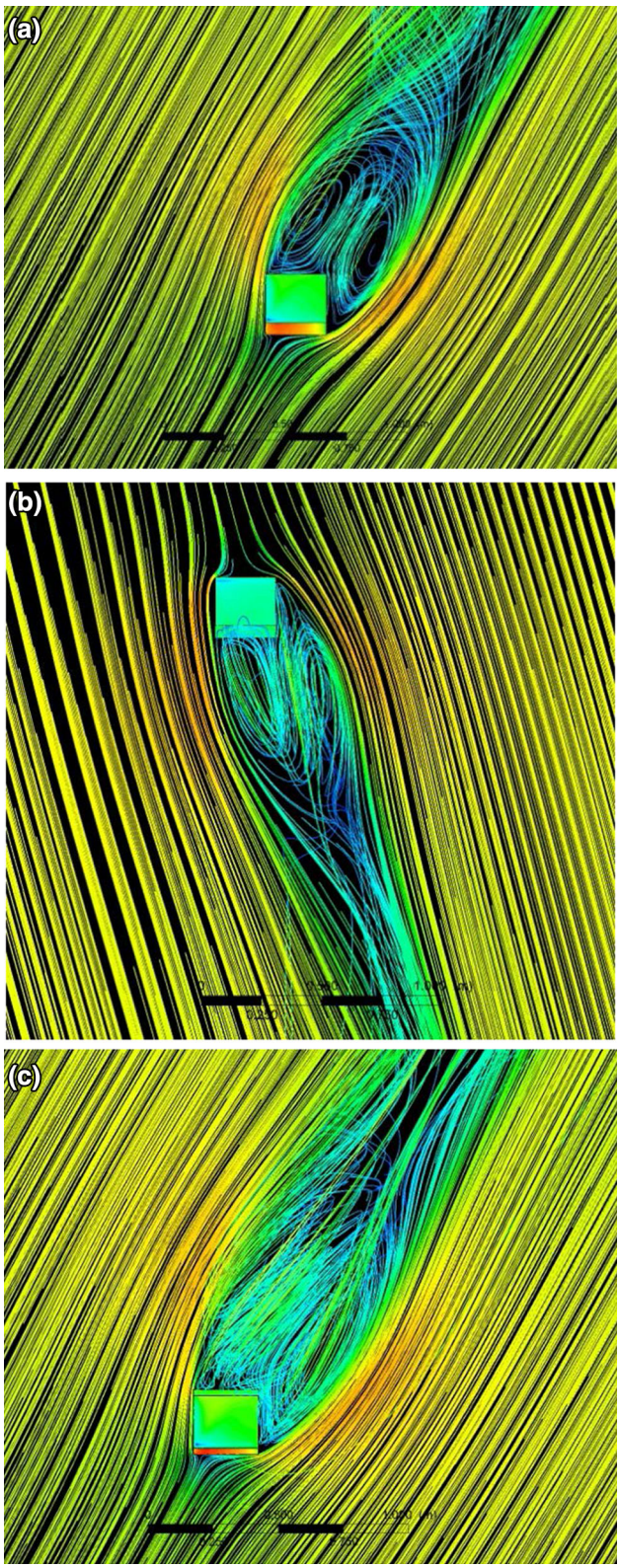

Fig. 13 Stream line for wind angles: **a** model A1, 30°, **b** model A1, 150°, and **c** model A2, 30°

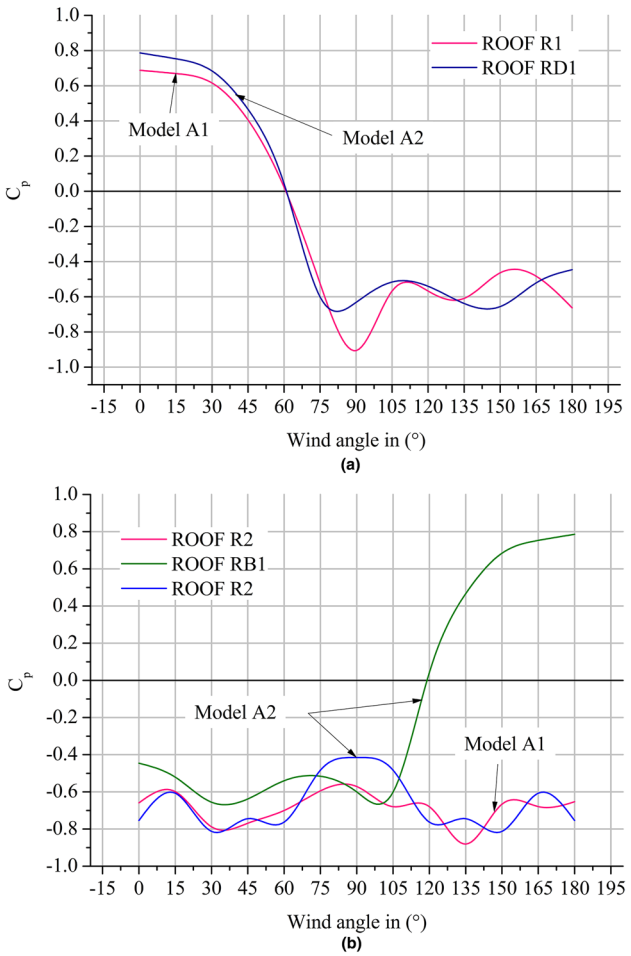

Fig. 14 Comparison of pressure coefficient for roof of model A1 and A2 due to different wind angles: **a** roof R1 and RB1; **b** roof R2 and RD1

from A1 and changed the sign. An important notable point in this case is no negative moment developed in any wind angle for A1 model, but for A2 model has negative moments between 0° to 15° and 165° to 180°. Therefore, it may be said that the maximum 259.02% extramoment develops on A2 model compared with A1 model for 90° angle and the reason is both-side setback of model A2. After all the experiments, it is concluded that both-side setback model is more vulnerable than the single-side setback model.

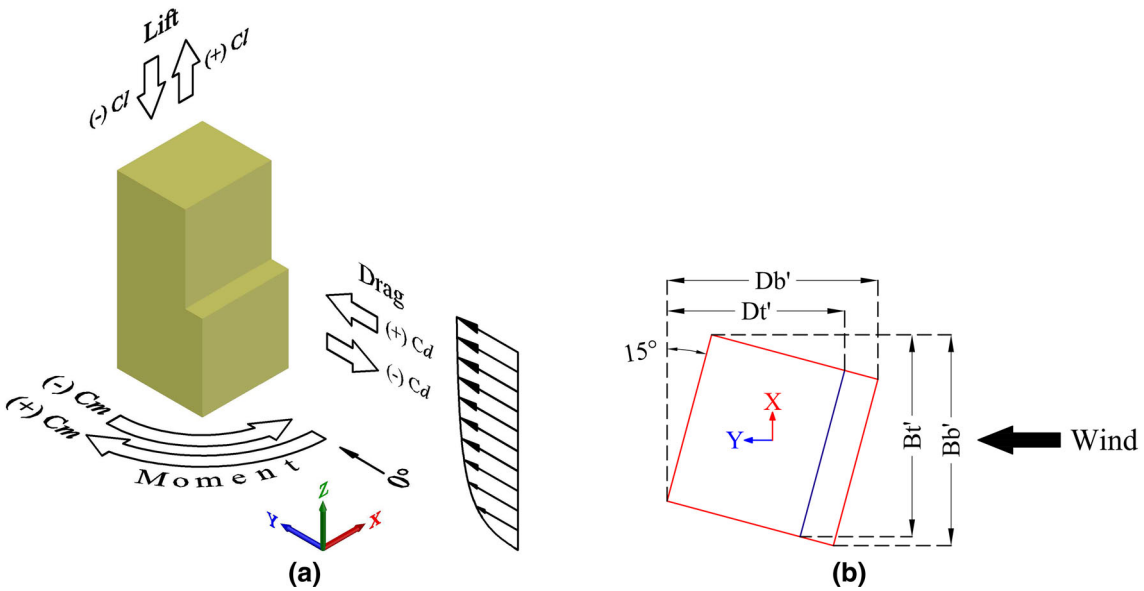

Fig. 15 **a** Diagram of drag, lift, and torsional moment coefficient; **b** projected width of the model due to rotation of wind

Conclusions

According to encyclopedic investigative studies on aerodynamic coefficient and structural behavior on setback tall building, the following results are obtained as follows.

1. The inspected angle between 0° to 180° at 15° interval has a special angle 150°, where the pressure coefficient at face A for model A1 experienced with high suction, whereas have extreme low suction at the same face for model A2. This drastic change of pressure is due to the setback on A2 model.
2. Suction are decreased to 79.60 and 76.19% for 30° and 150° angle on face B and D1 as compared between A1 and A2, respectively, at the ground portion. Again, 48.65% extrasuction noticed in A2 model at roof R2 and 19.13% positive pressure decreases at face B.
3. Maximum 13.24% drop of pressure has been observed at face B compared with two models for 150° angle. This type of extreme pressure fall not observed on other faces for this particular angle. Therefore, it may be said that this type of extreme pressure fall is due to the setback effect.
4. Pressure on roof R1 and R2 for model A1 has high suction compared with the roof R2 and RD1, respectively, for model A2 for that 150° angle. This type of pressure variation is due to the setback on both sides of model A2.
5. Maximum fluctuation of pressure between roof R1 and RD1 for model A1 and A2, respectively, is 14.25, 34.24, 41.38, and 32.73% for 0°, 90°, 150°, and 180° angles. Equivalently, maximum fall of suction between roof R2 for both the models is 27.32% for 90° angle.
6. Maximum drop of suction at roof R2 between A1 and A2 for 90° angle is 95.84%. After this study, it is clear that the model A2 established less suction for 0°, 90°, and 180° angles compared with the model A1 at setback roof R1 and 90° angle for roof R2.
7. Drag and lift force is increased to 274.11 and 206.84% for 135° and 180° angle, respectively, from A1 to A2.
8. According to the torsional moment comparison, the maximum torsional moment is 259.02% extra for 90° angle and 112.3% less moment for 180° angle from A1 to A2 model.
9. Finally, it is clear that the both-side setback model is more vulnerable than the single-side setback model.

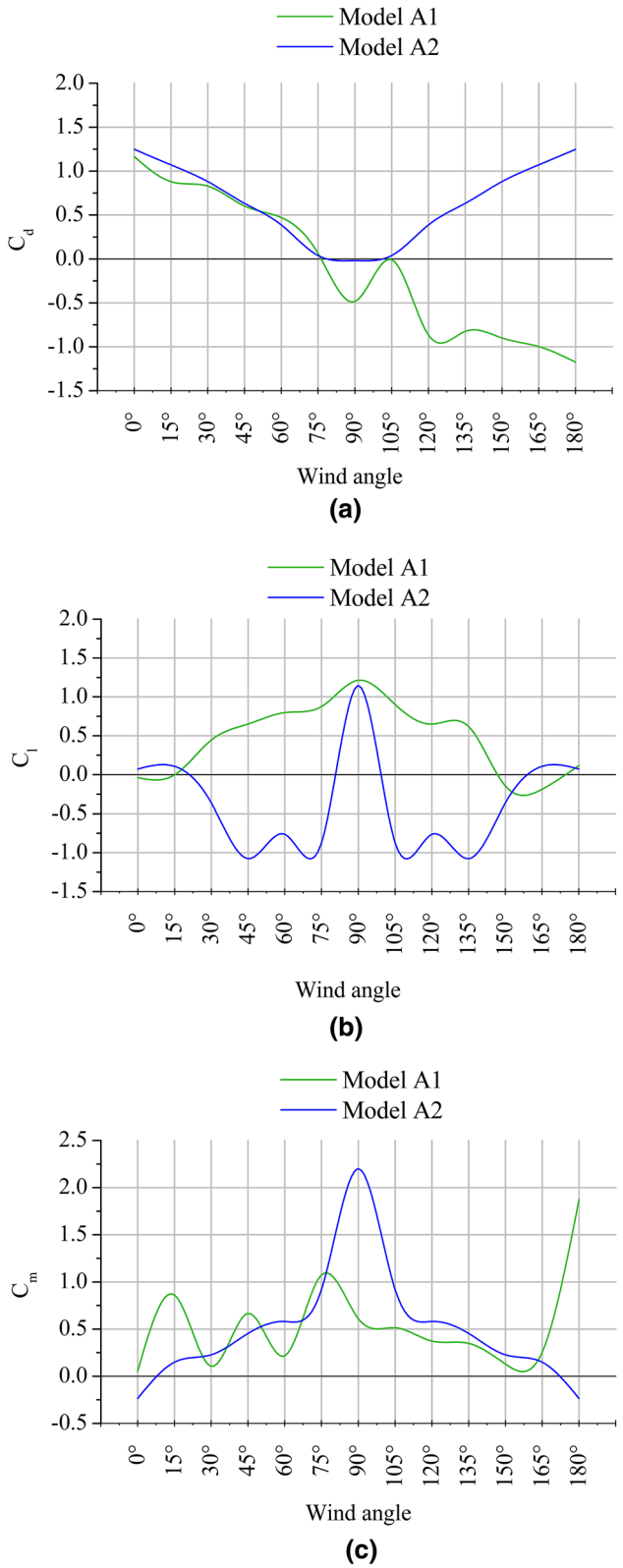

Fig. 16 Drag, lift, and torsional moment coefficients for model A1 and A1: **a** drag coefficient, **b** lift coefficient, and **c** torsional moment coefficient

References

ANSYS CFX-Solver Theory Guide. (October 2012). Release 14.5.

AS/NZS: 1170.2:2002. (2002). *Structural design actions, part 2: Wind actions*. Sydney, Wellington: Standards Australia/Standards New Zealand.

ASCE/SEI: 7-10:2010. (2010). *Minimum design loads for buildings and other structures*. Reston: Structural Engineering Institute of the American Society of Civil Engineering.

Baby, S., Jithin, P. N., & Thomas, A. M. (2015). A study of wind pressure on tall buildings and its aerodynamic modifications against wind excitation. *International Journal of Engineering Development and Research, 3,* 1–10.

BS 6399-2:1997. (1997). *British standard: Loading for buildings part 2. Code of practice for wind loads*. London: British Standard Institution.

Elshaer, A., Bitsuamlak, G., & Damatty, A. E. (2016). Aerodynamic shape optimization of tall buildings using twisting and corner modifications. In *Proceedings of the 8th International Colloquium on Bluff Body Aerodynamics and Application*. Boston. MA: Northeastern University.

EN 1991-1-4:2005/AC:2010(E). (2010). European committee for standardization (CEN). *Eurocode 1: Actions on structures-part 1–4: General actions—Wind actions. European Standard (Eurocode)*. Europe: European Committee for Standardization (CEN).

Franke, J., Hirsch, C., Jensen, A., Krüs, H., Schatzmann, M., Westbury, P., Miles, S., Wisse, J., & Wright, N. G. (2004). *Recommendations on the use of CFD in wind engineering. COST Action C14: Impact of wind and storm on city life and built environment*. Von Karman Institute for Fluid Dynamics.

Hossain, M. J., Islam, M. Q., & Ali, M. (2013). Lift and drag on cylinder of octagonal cross-section in a turbulent stream. *Journal of Engineering Science and Technology Review, 6,* 105–110.

Irwin, P., Kilpatrick, J., Robinson, J., & Frisque, A. (2008). Wind and tall buildings: Negatives and positives. *The Structural Design of Tall and Special Buildings, 17,* 915–928.

I.S: 875 (Part-3):2015. (2015). *Indian standard code of practice for the design loads (other than earthquake) for buildings and structures (part-3. wind loads)*. New Delhi, India: Bureau of Indian Standards.

Kareem, A. (1992). Dynamic response of high-rise buildings to stochastic wind loads. *Journal of Wind Engineering and Industrial Aerodynamics, 41,* 1101–1112.

Kijewski-Correa, T., & Pirnia, J. D. (2007). Dynamic behaviour of tall buildings under wind: Insights from full-scale monitoring. *The Structural Design of Tall and Special Buildings, 16,* 471–486.

Kim, Y. C., & Kanda, J. (2013). Wind pressures on tapered and set-back tall buildings. *Journal of Fluids and Structures, 39,* 306–321.

Kim, Y. M., You, K. P., & Ko, N. H. (2008). Across-wind responses of an aeroelastic tapered tall building. *Journal of Wind Engineering and Industrial Aerodynamics, 96,* 1307–1319.

Kumar, H. S., Rajan, S. S., Andrew, A. J., Babu, G. R., Raoa, N. S., & Jawahar, J. G. (2016). Aerodynamic coefficients for a rectangular tall building under sub-urban terrain using wind tunnel. *Asian Journal of Civil Engineering (BHRC), 17,* 325–333.

Kwon, D. K., & Kareem, A. (2013). Comparative study of major international wind codes and standards for wind effects on tall buildings. *Engineering Structures, 51,* 23–35.

Masera, D., Ferro, G. A., Persico, R., Sarkisian, M., Beghini, A., Macheda, F., & Froio, M. (2015). Effect of wind loads on non-regularly shaped high-rise buildings. *Proceedings of the 40th*

Conference on our World in Concrete & Structures (pp. 1–9), Singapore.

Mendis, P., Mohotti, D., & Ngo, T. (2014). Wind design of tall buildings, problems, mistakes and solutions. In *Proceedings of the 1st International Conference on Infrastructure Failures and Consequences*. Melbourne, Australia.

Mendis, P., Ngo, T., Haritos, N., Hira, A., Samali, B., & Cheung, J. (2007). Wind loading on tall buildings. *Electronic Journal of Structural Engineering. Special Issue: Loading on Structures, 3,* 41–54.

Revuz, J., Hargreaves, D. M., & Owen, J. S. (2012). On the domain size for the steady-state CFD modelling of a tall building. *Wind and Structures, 15,* 313–329.

Roy, K., & Bairagi, A. K. (2016). Wind pressure and velocity around stepped unsymmetrical plan shape tall building using CFD simulation—A case study. *Asian Journal of Civil Engineering (BHRC), 17,* 1055–1075.

Shiva, A. K. A., & Gupta, P. K. (2013). Wind loads on tall buildings with steps. *Journal of Academia and Industrial Research, 1,* 766–768.

Simiu, E., & Scanlan, R. H. (1996). *Wind effects on structures fundamentals and applications to design (3rd ed.)*. New York: Wiley.

S.P 64 (S&T):2001. (2001). *Explanatory hand book on Indian standard code of practice for design loads (other than earthquake) for buildings and structures, part 3 wind loads [IS 875 (part 3): 1987]*. New Delhi, India: Bureau of Indian Standards.

Tamur, Y., Xua, X., Tanakac, H., Kima, Y. C., Yoshidaa, A., & Yangd, Q. (2017). Aerodynamic and pedestrian-level wind characteristics of super-tall buildings with various configurations. In *Proceedings of the 10th International Conference on Structural Dynamics, EURODYN, Procedia Engineering* (Vol. 199, pp. 28–37).

Tanaka, H., Tamura, Y., Ohtake, K., Nakai, M., Kim, Y. C., & Bandi, E. K. (2013). Aerodynamic and flow characteristics of tall buildings with various unconventional configurations. *International Journal of High-Rise Buildings, 2,* 213–228.

Weerasuriya, A. U., & Jayasinghe, M. T. R. (2014). Wind loads on high-rise buildings by using five major international wind codes and standards. *Engineer: Journal of the Institution of Engineers, 3,* 13–25.

Xie, J. (2014). Aerodynamic optimization of super-tall buildings and its effectiveness assessment. *Journal of Wind Engineering and Industrial Aerodynamics, 130,* 88–98.

Xu, Z., & Xie, J. (2015). Assessment of across-wind responses for aerodynamic optimization of tall buildings. *Wind and Structures, 21,* 505–521.